J Mater Sci: Mater Electron (2021) 32:22813–22821

Crystal structure, microwave dielectric properties, and dielectric resonant antenna studies of novel low-permittivity $CoAl_2O_4$ spinel ceramics

Yi Ding[1], Cheng Chao Hu[2], Wei Qin Sheng[1], Kai Xin Song[1], and Bing Liu[1,*]

[1] College of Electronic Information and Engineering, Hangzhou Dianzi University, Hangzhou, China
[2] College of Materials Science and Engineering, Liaocheng University, Liaocheng, China

Received: 29 June 2021
Accepted: 4 August 2021
Published online: 16 August 2021

ABSTRACT

$CoAl_2O_4$ spinel ceramics were prepared via a standard solid-state reaction method, and their crystal structure, microwave dielectric properties, and dielectric resonant antenna applications were systematically investigated in this study. X-Ray diffraction patterns and Raman spectra confirmed that $CoAl_2O_4$ belongs to the *Fd*-3 *m* space group with cubic crystal symmetry. ε_r and *Qf* values increased with the increasing sintering temperature, where an ever-improving microstructure was also observed from the scanning electron micrographs. The optimal microwave dielectric properties were achieved as follows: ε_r = 9.34, *Qf* = 30,500 GHz, and $\tau_f = -54$ ppm/°C. Moreover, a dielectric resonant antenna was designed and simulated to demonstrate the application prospects of $CoAl_2O_4$ ceramics towards microwave antennas. The $CoAl_2O_4$-based antenna resonating at 14.33 GHz exhibited a high return loss of −40.9 dB, a wide impedance bandwidth of 940 MHz, and an exceptionally high total efficiency of 96.6%. The remarkable antenna performances suggested that $CoAl_2O_4$ ceramics were promising candidates for wireless communication devices operating at the *Ku*-band, provided τ_f can be further tuned toward zero.

1 Introduction

Wireless communication technology is fundamental to how we live, work, and play in the increasingly digital world. This trend has been building for decades and came to a head during the COVID-19 pandemic, when millions of us have come to depend on networks for packaged goods, entertainment, work—and still expect nearly immediate gratification. To meet those needs, the operating frequency of communication is expanding to the millimeter-wave region to offer a more efficient, secure, and flexible network [1, 2]. Microwave dielectric ceramics are critical components in wireless communication devices owing to the merits of low cost, excellent dielectric properties, and good thermal conductivity

Address correspondence to E-mail: liubing@hdu.edu.cn

https://doi.org/10.1007/s10854-021-06760-2

[3, 4]. The dielectric permittivity (ε_r), quality factor (Qf), and temperature coefficient of resonant frequency (τ_f) are three fundamental parameters in evaluating microwave dielectric properties. For millimeter-wave applications, a low-permittivity ($\varepsilon_r < 10$) is preferred for high-speed signal transmission with minimum attenuation [5–7]. Moreover, high Qf and near-zero τ_f values are always desirable for satisfactory resonant frequency selectivity and temperature stableness, respectively.

Aluminates are promising low-ε_r candidates owing to the relatively low ionic polarizability of Al^{3+} (0.79 $Å^3$) [8]. Among these, spinels with the general formula of MAl_2O_4 (M = transition metals) have been extensively investigated owing to their easy preparation and low dielectric loss [9, 10]. Surendran et al. reported the microwave dielectric properties of $ZnAl_2O_4$ ceramics for the first time, where the optimal properties (ε_r = 8.5, Qf = 56,300 GHz, τ_f = −79 ppm/°C) were obtained when sintered at 1425 °C [9]. Meanwhile, similar microwave dielectric properties with ε_r = 8.75, Qf = 68,900 GHz, and τ_f = −75 ppm/°C were also obtained in $MgAl_2O_4$ ceramics [10]. On the other hand, the spinel structure is flexible to substitutions. Numerous cations and cation combinations can be accommodated to obtain extremely diversified spinel end-members [11, 12]. However, current studies on the dielectric properties of spinels are mainly focused on the most common Mg- and Zn-based compounds. Systematic studies on different spinel end-members are lacking in the literature.

Owing to the similar ionic radius of Co^{2+} (0.65 Å) and Mg^{2+} (0.67 Å), the substitution of Co^{2+} for Mg^{2+} has been widely conducted and confirmed effective in improving the sinterability and microwave dielectric properties. By partially substituting Mg with Co, Huang et al. reported that the $(Mg_{1-x}Co_x)$-Ti_2O_4 ceramics possess much higher Qf values than the Mg-end member [13]. For Mg-based spinels, Tsai et al. reported a significant improvement of Qf value by forming $(Mg_{1-x}Co_x)Al_2O_4$ solid solutions as well [14]. Meanwhile, Tsai et al. reported similar low-ε_r values of around 9 in $CoAl_2O_4$ spinel ceramics as well [14], while a systematical investigation on their sintering behavior, structure, microwave dielectric properties and antenna applications is still lacking in the literature.

In this study, $CoAl_2O_4$ ceramics are prepared via a standard solid-state reaction method. The sintering behavior, crystal structure, microstructure are systematically investigated together with their effects on the microwave dielectric properties. Moreover, a $CoAl_2O_4$-based dielectric resonator antenna prototype is designed and simulated to further explore their antenna applications.

2 Experimental procedure

$CoAl_2O_4$ ceramics were prepared via a standard solid-state reaction method using high-purity CoO (99.99%) and Al_2O_3 (99.99%) powder as raw materials. First, the stoichiometrically weighted powder was ball-milled in ethanol media for 12 h. After drying, the mixture was sieved and then calcined at 1200 °C for 3 h. Next, the calcined powder was re-milled and then pressed into pellets with 12 mm in diameter and 5 mm in height. Finally, the green pellets were sintered at 1450–1550 °C for 3 h to obtain the dense $CoAl_2O_4$ ceramics.

The relative density of $CoAl_2O_4$ ceramics was evaluated using the Archimedes method. Room-temperature X-ray diffraction (XRD) patterns were collected using a Shimadzu XRD-700X diffractometer. The XRD data for Rietveld analysis was collected using the step-scan mode, with a step degree of 0.02° and a counting time of 2 s. The ceramic samples were carefully polished to a roughness of about 0.5 μm for Raman measurement. Room-temperature Raman spectra were recorded using an HR-800 LabRaman device (Jobin Yvon, Longjumeau, France). Ar^+ ion laser with an output power of 20mW was used as the excitation source. The polished and thermal etched surfaces of $CoAl_2O_4$ ceramics were observed using an S-3400 (Hitachi, Tokyo, Japan) scanning electron microscopy (SEM). The thermal etching process was carried out at 50 °C lower than the sintering temperature for 0.5 h. The dimensions of the sintered $CoAl_2O_4$ ceramics were around 9.5 mm in diameter and 5 mm in height. The measured resonant frequency of the $CoAl_2O_4$ ceramics was around 11 GHz. The Qf value was evaluated by the resonant-cavity method [15], using a silver-coated cavity connected to an E8363B network analyzer (Agilent, Palo Alto, CA). ε_r and τ_f values were measured using the parallel-plate method [16]. The measurement of τ_f value was organized in the temperature range of 20–80 °C. The design and simulation of the dielectric resonant antenna were conducted using the commercially

available Computer Simulation Technology (CST) software.

3 Result and discussion

Figure 1 shows the relative density of $CoAl_2O_4$ ceramics as a function of sintering temperature. $CoAl_2O_4$ ceramics exhibit a relatively large sintering temperature range, as dense ceramics with relative densities above 94.5% are achieved in the whole sintering temperature range. An abrupt increase of relative density from 94.7% at 1475 °C to 97.3% at 1500 °C is noticed and remains relatively stable with further increasing sintering temperature. On the other hand, $CoAl_2O_4$ spinels are commonly investigated as ceramic pigments owing to their intense blue color and peculiar optical properties [17, 18]. As shown in the inset of Fig. 1, the color of $CoAl_2O_4$ ceramics turns from navy blue at 1450 °C to dark blue at 1500 °C and 1550 °C, which further confirms the improvement of relative density with increasing sintering temperature.

Figure 2a shows the XRD patterns of $CoAl_2O_4$ ceramics sintered at various temperatures. All the diffraction patterns match well with the standard diffraction feature of $CoAl_2O_4$ (JCPDS card No. 44–0160), and the relevant indices of crystallographic planes are labeled. Furthermore, no apparent change of peak position and intensity is observed with the increasing temperature. Hence, monophasic $CoAl_2O_4$ ceramics have been successfully prepared in this

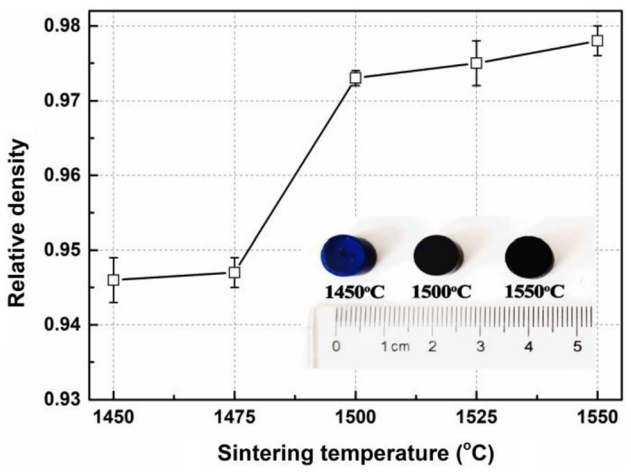

Fig. 1 The relative density of $CoAl_2O_4$ ceramics as a function of sintering temperature. The inset shows an optical photograph of the sintered ceramics

study, and the crystal structure remains stable in the whole temperature range. To further explore the crystal structure, the XRD data of $CoAl_2O_4$ ceramics sintered at 1550 °C is refined based on the spinel structure with a space group of *Fd*-3 *m*. Figure 2b shows the measured and calculated diffraction profiles of $CoAl_2O_4$ ceramics. The refined atomic coordinates, thermal displacement parameters, and occupations are listed in Table 1.

The measured and calculated XRD patterns keep a good consistency, as confirmed by the flatness of the difference line (Yobs-Ycal). Moreover, the outstanding reliability factors (R_p = 0.839%, R_{wp} = 1.13%, R_{exp} = 0.73%, and χ^2 = 2.37) indicate that the adopted spinel structure is valid and the refined results are reliable. Based on the refined structural parameters, Fig. 3 demonstrates the crystal structure of $CoAl_2O_4$. There are two kinds of Wyckoff positions for cations, i.e., 8a (1/8, 1/8, 1/8) and 16d (1/2, 1/2, 1/2). The cations connect with the neighboring oxygen anions and form two types of oxygen polyhedrons (i.e., tetrahedron at 8a site and octahedron at 16d site). On the other hand, the structural formula of $CoAl_2O_4$ can also be expressed as $^{IV}(Co_{1-x}Al_x)^{VI}[Co_xAl_{2-x}]O_4$, where $^{IV}()$ and $^{VI}[]$ represent the 8a and 16d site, respectively; x is called the inversion parameter [19, 20]. For normal spinels such as $ZnAl_2O_4$ and $MgAl_2O_4$, x equals 0. A value of x = 2/3 corresponds to a completely random cation distribution between 8a and 16d sites. The other spinels with x between 0 and 2/3 are denoted as largely normal spinels or between 2/3 and 1 (largely inverse spinels). According to the occupation results listed in Table 1, $CoAl_2O_4$ ceramics is a largely normal spinel with the calculated x value of 0.098. Co^{2+} has a strong preference for tetrahedral 8a site and Al^{3+} for octahedral 16d site, though the cation radius of Al^{3+} (0.535 Å) is smaller than that of Co^{2+} (0.65 Å).

On the other hand, Raman spectroscopy is a powerful tool in revealing information on the crystal structure, electronic structure, and lattice vibrations [21–23]. Figure 4 plots the Raman spectra of $CoAl_2O_4$ ceramics sintered at 1450 °C and 1550 °C, respectively. Both samples display similar Raman patterns with five obvious Raman active peaks. No apparent change of peak position and intensity is noticed, corresponding to the similar XRD patterns obtained at various sintering temperatures. For spinels, the irreducible representations that describe the vibration

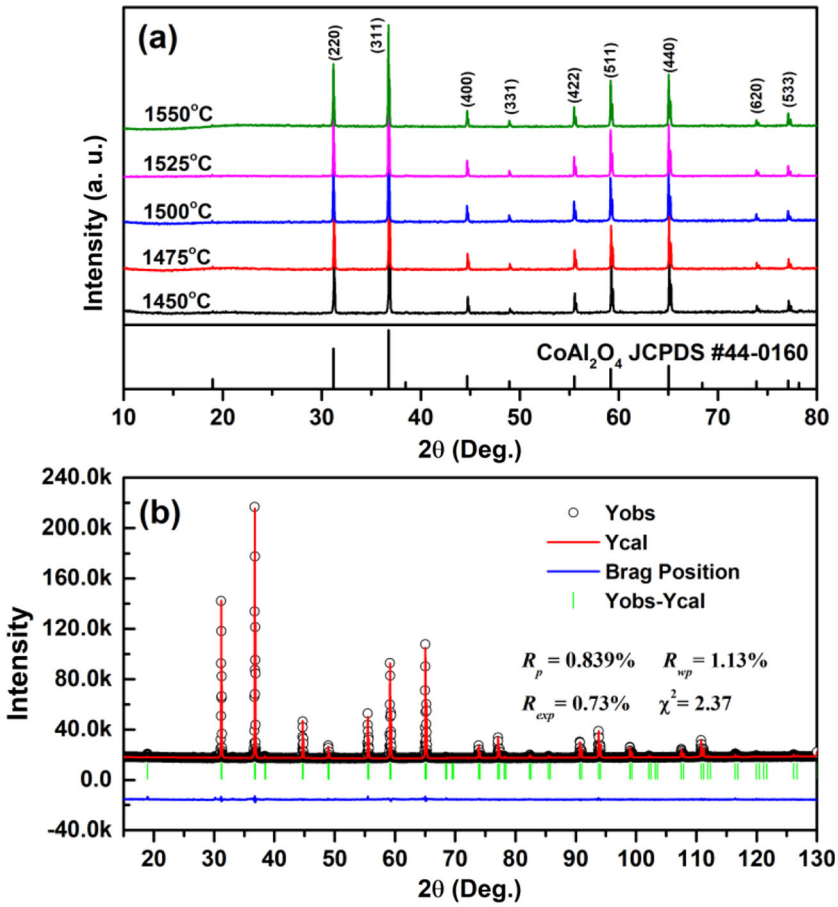

Fig. 2 **a** The XRD patterns of $CoAl_2O_4$ ceramics sintered at various temperatures. **b** The measured (circles) and Rietveld refined (red line) XRD patterns of $CoAl_2O_4$ ceramics sintered at 1550 °C. The green short vertical lines mark the Brag peak positions

Table 1 The Wyckoff positions, refined atomic coordinates, thermal displacement parameters, and occupations for $CoAl_2O_4$ ceramics

Cation	site	*x*	*y*	*z*	*Biso*	*Occ*
Co1	8a	0.1250	0.1250	0.1250	0.6159	0.2254
Al1	8a	0.1250	0.1250	0.1250	0.6159	0.0246
Co2	16d	0.5000	0.5000	0.5000	0.7263	0.0246
Al2	16d	0.5000	0.5000	0.5000	0.7263	0.4754
O1	32e	0.2648	0.2648	0.2648	0.7663	1.0000

modes of each Wyckoff position can be written as follows [11, 24]:

$$\text{8a site}: \ F_{1u}(IR) + F_{2g}(R)$$

$$\text{16d site}: \ A_{2u}(S) + E_u(S) + F_{2u}(S) + 2F_{1u}(IR)$$

$$\text{32e site}: A_{1g}(R) + A_{2u}(S) + E_u(S) + E_g(R) + 2F_{2g}(R) + F_1(S) + F_{2u}(S) + 2F_{1u}(IR)$$

where the (R) and (IR) denote Raman- and infrared-active vibrational modes, respectively. The rest modes marked with (S) are silent. Therefore, the Raman active modes of $CoAl_2O_4$ ceramics are $3F_{2g} + A_{1g} + E_g$. Besides, the three $3F_{2g}$ modes are labeled as $F_{2g}(1)$, $F_{2g}(2)$, and $F_{2g}(3)$ based on their wavenumbers.

The wavenumbers of the Raman active peaks are obtained via fitting the spectra using a Lorentz function, and the results are consistent with the previous works [25–27]. The $F_{2g}(1)$ mode at 202 cm^{-1} is assigned to the Co/Al-O_4 tetrahedron translation [25]. The position of E_g mode is reported to have a reasonable correlation with the cation radius at the 8a site [11]. Hence, the E_g mode at 409 cm^{-1} is assigned to the symmetric bending motion of the oxygen atoms within the tetrahedron [26]. The $F_{2g}(2)$ mode at 517 cm^{-1} is attributed to the Co/Al-O asymmetric stretching vibration in the tetrahedral sites [11, 26]. The literature is inconsistent regarding the vibration assignment for the $F_{2g}(3)$ mode at 629 cm^{-1}, which has been reported as either the anti-symmetric

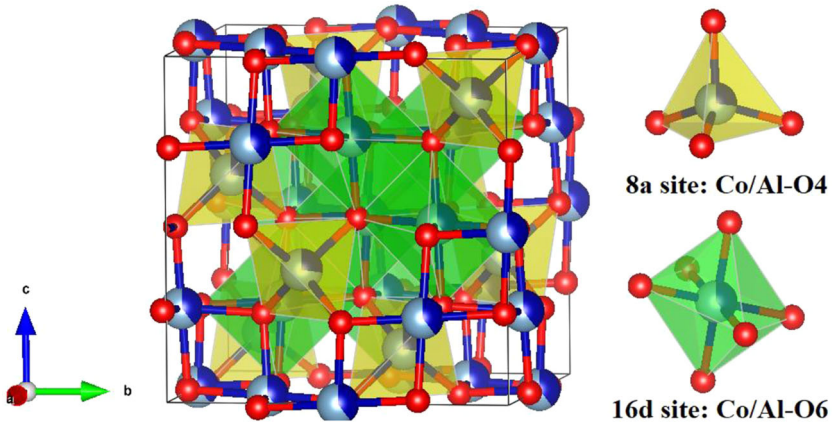

Fig. 3 The crystal structure of $CoAl_2O_4$ spinel ceramics

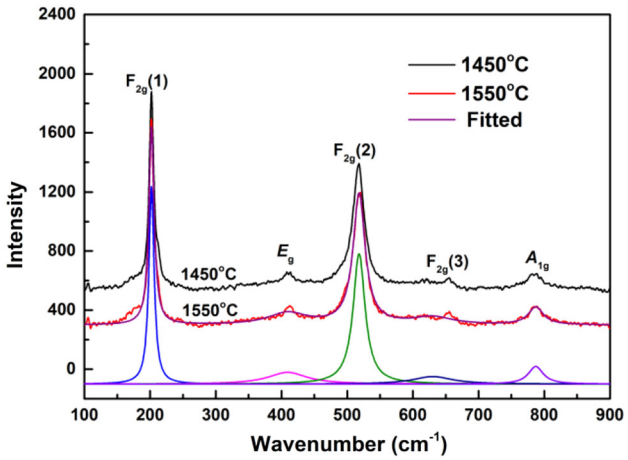

Fig. 4 Raman spectra of $CoAl_2O_4$ ceramics sintered at 1450 °C and 1550 °C

stretching mode of the tetrahedron unit or an asymmetric bending motion of the oxygen bonded to the tetrahedral cation [27, 28]. Previous studies on the wavenumber of A_{1g} mode demonstrate that the octahedral cation has a more significant effect than the tetrahedral cation [29, 30]. This justifies that the A_{1g} mode at 785 cm^{-1} is related to the Co/Al-O stretching vibration in the octahedron.

Figure 5 shows the SEM images and corresponding grain size distributions of $CoAl_2O_4$ ceramics sintered at various temperatures. The microstructure is getting dense with the increasing sintering temperature. Besides, an apparent increase of grain size from 0.88 μm at 1450 °C to 5.10 μm at 1550 °C is also noticed. The improvement of microstructure is in good agreement with the variation of relative density and should be mainly attributed to the increased driving force of grain growth.

Figure 6 shows the microwave dielectric properties of $CoAl_2O_4$ ceramics as functions of sintering temperature. ε_r increases monotonously with the increasing sintering temperature, from 8.959.34 °C at 1450 °C to 9.34 °C at 1550 °C. The variation of ε_r is in good agreement with the relative density, indicating that ε_r should be mainly determined by the porosity (P). According to Alford et al. [31], the effect of porosity can be excluded using the following Eq. (1), and the porosity corrected values (ε_{cor}) are plotted in Fig. 6a. All the ε_{cor} values maintain at around 9.6, confirming that the porosity mainly dominates ε_r of the present ceramics.

$$\varepsilon_r = \varepsilon_{cor}\left(1 - \frac{3P(\varepsilon_{cor} - 1)}{2\varepsilon_{cor} + 1}\right) \quad (1)$$

Qf value indicates a monotonous increase with the increasing sintering temperature, from 23,550 GHz at 1450 °C to 30,500 GHz at 1550 °C. Since no phase transformation is obtained as confirmed from the XRD patterns, the increase of Qf value should be mainly attributed to the optimization of microstructures as shown in the SEM images. The optimal Qf value of $CoAl_2O_4$ ceramics is lower than the normal spinels such as $ZnAl_2O_4$ (56,300 GHz) and $MgAl_2O_4$ (68,900 GHz). According to Tsai et al., the lower Qf value in $CoAl_2O_4$ ceramics should be attributed to the more random distributions of the cations occupying tetrahedral and octahedral sites, which could render the anharmonic phonon decay process in the ceramic crystal and degrade the quality factors [14]. The variation of τ_f value is insensitive to the sintering temperature, and all the values maintain at around −54 ppm/°C. The negative τ_f value of the present ceramics poses difficulties for practical applications, which can be further optimized via forming

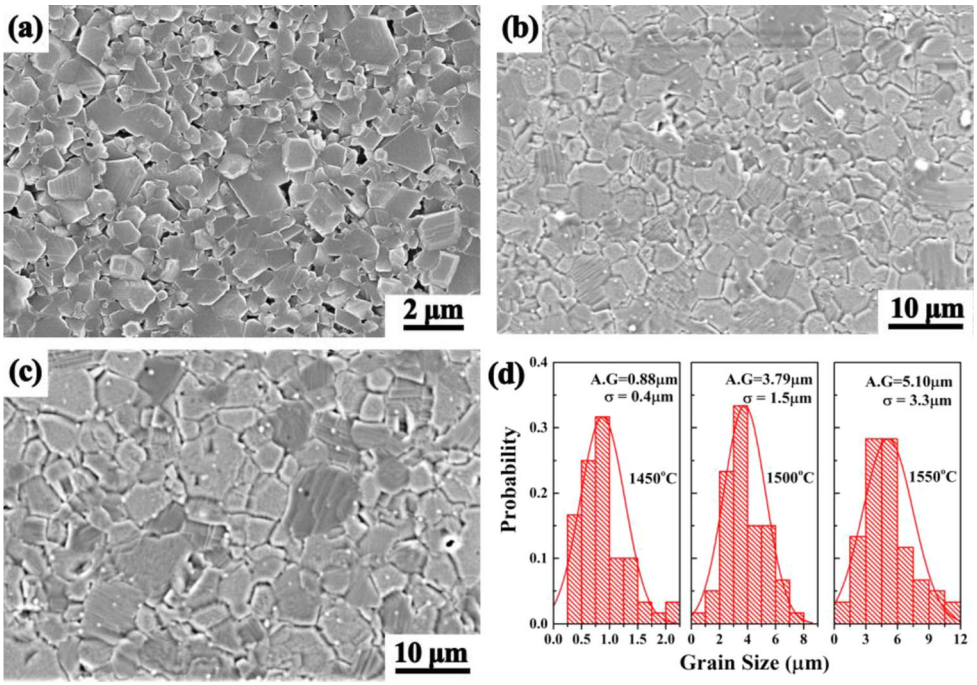

Fig. 5 SEM images of the polished and thermal etched surfaces of $CoAl_2O_4$ ceramics sintered at various temperatures, **a** 1450 °C, **b** 1500 °C, and **c** 1550 °C. **d** The corresponding grain size distributions and average grain size of $CoAl_2O_4$ ceramics

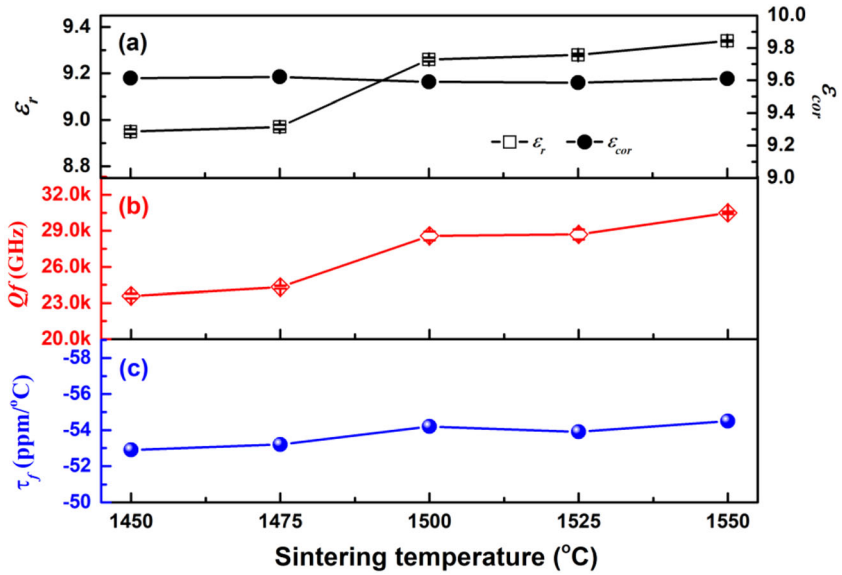

Fig. 6 The microwave dielectric properties (**a**) ε_r, (**b**) Qf, and (**c**) τ_f values of $CoAl_2O_4$ ceramics sintered at various temperatures

composite ceramics with components having positive τ_f values, such as TiO_2 ($\tau_f = +460$ ppm/°C), $CaTiO_3$ ($\tau_f = +850$ ppm/°C) [32, 33]. The optimal microwave dielectric properties with $\varepsilon_r = 9.34$, $Qf = 30{,}500$ GHz, and $\tau_f = -54$ ppm/°C are obtained when sintered at 1550 °C.

A dielectric resonator antenna (DRA) consists of a block of ceramic (dielectric resonator) mounted on a metal surface (ground plane). DRA offers attractive features compared to microstrip patch antennas, including higher gain and efficiency, wider bandwidth, and easier excitation [34, 35].

A $CoAl_2O_4$-based DRA prototype is designed using the microstrip-slot coupling scheme. Figure 7 demonstrates the configuration of the proposed DRA, and the dimensions are listed in Table 2. A 40 × 40 × 1 mm FR4 substrate is pasted with copper foil (thickness: ~ 0.06 mm) on one side as conducting ground plane. A cylindrical $CoAl_2O_4$-based dielectric resonator (DR) with a diameter of 9.5 mm and height of 4.8 mm is placed over an etch slot in the

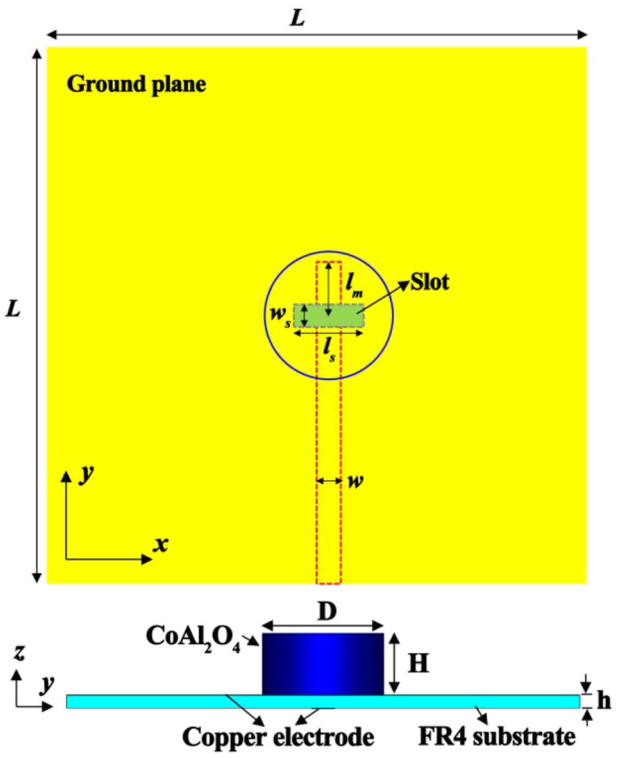

Fig. 7 Top and side view of the designed DRA using a microstrip-slot coupling scheme

Table 2 The dimensions of the designed rectangular DRA

Parameter name	Parameter	Value (mm)
DRA-diameter	D	9.5
DRA-height	H	4.8
Substrate-length	L	40
Substrate-height	h	1
Slot length	l_s	5.2
Slot width	w_s	1.7
Microstrip line width	w	1.8
GP side width	l_m	4

ground plane. The fields of the microstrip line "leak" through the slot to excite the DR.

Figure 8 shows the simulated antenna performances of the $CoAl_2O_4$-based DRA. The S_{11} parameter is a measure of impedance mismatch and reflects how much power is reflected from the antenna. The minimum S_{11} parameter is generally achieved at the resonant frequency. Meanwhile, for practical applications, the S_{11} values should be lower than −10 dB in the whole operating frequency range [36, 37]. As shown in Fig. 8a, the designed DRA resonates at the *Ku*-band region, where an excellent S_{11} of −40.9 dB is obtained at the resonant frequency of 14.33 GHz. Besides, a considerably large impedance bandwidth (the frequency range where S_{11} is below −10 dB) of 940 MHz is also achieved, which surpasses those reported in microstrip patch antennas [1, 2, 38]. The voltage standing wave ratio (VSWR) is another indicator of impedance mismatch. The VSWR value at the resonant frequency should be close to unity for proper working [37]. As shown in Fig. 8b, the designed DRA exhibits an excellent VSWR of 1.03 at 14.33 GHz and is found to be less than 2 in the entire impedance bandwidth frequency range. Figure 8c shows the total efficiency of the DRA as a function of frequency, where a maximum value of 96.6% is obtained at the resonant frequency. The superior total efficiency surpasses the commercial antenna products (typically ranges from 20% to 70%) and indicates extensive application prospects [38, 39]. Finally, antenna gain is another critical parameter measuring the power radiated in a particular direction. Figure 8d demonstrates the three-dimensional (3D) polar plot of the radiation pattern, and the maximum gain is found to be 5.42 dB. A comparative table on the antenna performances is presented in Table 3. The comparative data suggests that the $CoAl_2O_4$-based DRA exhibits superior antenna properties, including S_{11} parameters, bandwidth, and total efficiency, compared to the reported work.

4 Conclusions

In this study, single-phase $CoAl_2O_4$ ceramics have been successfully prepared via a standard solid-state reaction method. XRD and Raman results demonstrate that $CoAl_2O_4$ crystallizes in a largely normal spinel structure with a space group of *Fd*-3 *m*. The SEM images show an ever-optimizing microstructure with the increasing sintering temperature, which is beneficial to the improvement of ε_r and *Qf* values. The optimal microwave dielectric properties (ε_r = 9.34, *Qf* = 30,500 GHz, and τ_f = −54 ppm/°C) are achieved when sintered at 1550 °C. A dielectric resonator antenna is designed using $CoAl_2O_4$ ceramics as the antenna element. The outstanding S_{11} (−40.9 dB) and VSWR (1.03) values at the resonant frequency of 14.33 GHz indicate a good impedance matching. Moreover, the S_{11} curve exhibits a large impedance bandwidth of 950 MHz, and the total

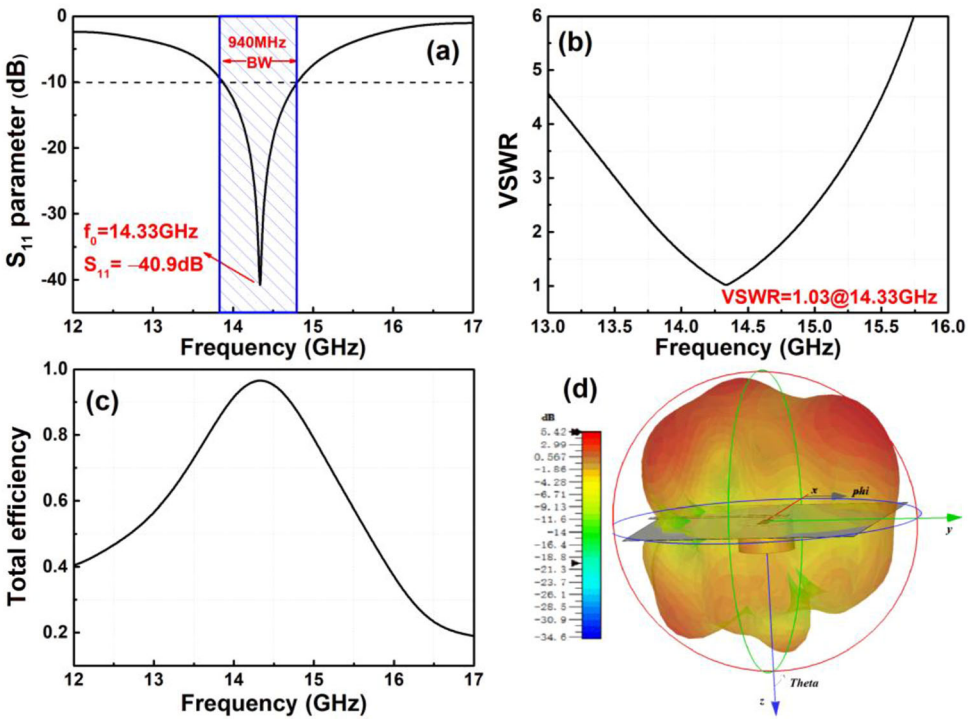

Fig. 8 The simulated antenna performances **a** S_{11} parameter, **b** VSWR, and **c** total efficiency of $CoAl_2O_4$-based DR antenna as functions of frequency. **d** The simulated 3D radiation patterns of $CoAl_2O_4$-based DR antenna

Table 3 Comparison of performances of recently reported antennas

Antenna material/type	Resonant frequency (GHz)	S_{11} (dB)	Bandwidth (MHz)	Gain (dB)	Total efficiency	References
LiF ceramics/microstrip patch antenna (MPA)	6.81	−20.3	148	4.5	90.5%	[1]
$SrGa_2O_4$ ceramics/MPA	4.80	−23.56	\	2.9	72.8%	[2]
Spinel-olivine composite ceramic /MPA	5.7	−14	80	\	59%	[38]
BaF_2 ceramics/MPA	5.78	−16.5	96	5.84	91.6%	[39]
$Li_2Ti_{0.75}(Mg_{1/3}Nb_{2/3})_{0.25}O_3$ ceramics /DRA	10.03	\	416	5.54	\	[34]
$MgAl_2O_4$ transparent ceramic /DRA	6.8	\	735	5.45	\	[35]
$SrFe_{12}O_{19}$ − Li_2MoO_4 composite /ferrite resonator antenna	12.89	−40	510	5.71	\	[37]
$CoAl_2O_4$ ceramics/ DRA	14.33	−40.9	940	5.42	96.6%	This work

efficiency at the resonant frequency is 96.6%. The excellent antenna performance suggests that $CoAl_2O_4$ ceramics have prospects of extensive applications in wireless communication devices operating at the *Ku*-band, provided τ_f can be further tuned toward zero.

Acknowledgements

This work was supported by the National Natural Science Foundation of China (51802062), the Fundamental Research Funds for the Provincial Universities of Zhejiang (GK219909299001-408), and the Natural Science Foundation of Zhejiang Province (ZJ2020008).

Declarations

Conflict of interest The authors declare no conflicts of interest.

References

1. B. Liu, K. Sha, C.C. Hu, Y.Q. Jia, L. Li, D. Zhou, D.W. Wang, K.X. Song, Y.H. Huang, J. Eur. Ceram. Soc. **41**, 4835 (2021)
2. B. Liu, K. Sha, M.F. Zhou, K.L. Zheng, W.C. Lou, K.W. Xu, K.X. Song, C.C. Hu, Y.H. Huang, J. Eur. Ceram. Soc. **41**, 5170 (2021)
3. H. Li, X. Chen, Q. Xiang, B. Tang, J. Lu, Y. Zou, S. Zhang, Ceram. Int. **45**, 14160 (2019)
4. H. Li, P. Zhang, S. Yu, H. Yang, B. Tang, F. Li, S. Zhang, Ceram. Int. **45**, 11639 (2019)
5. B. Liu, L. Li, K.X. Song, M.M. Mao, Z. Lu, G. Wang, L. Li, D. Wang, D. Zhou, A. Feteira, I.M. Reaney, J. Eur. Ceram. Soc. **41**, 1726 (2021)
6. H. Ohsato, J. Varghese, A. Kan, J.S. Kim, I. Kagomiya, H. Ogawa, M.T. Sebastian, H. Jantunen, Ceram. Int. **47**, 2735 (2021)
7. D. Zhou, L.X. Pang, D.W. Wang, Z.M. Qi, I.M. Reaney, A.C.S. Sustain, Chem. Eng. **6**, 11138 (2018)
8. B. Liu, C.C. Hu, Y.H. Huang, H.B. Bafrooei, K.X. Song, J. Alloy Compd. **791**, 1033 (2019)
9. K.P. Surendran, N. Santha, P. Mohanan, M.T. Sebastian, Eur. Phys. J. B **41**, 301 (2004)
10. K.P. Surendran, P.V. Bijumon, P. Mohanan, M.T. Sebastian, Appl. Phys. A **81**, 823 (2005)
11. V. D'Ippolito, G.B. Andreozzi, D. Bersani, P.P. Lottici, J. Raman Spectrosc. **46**, 1255 (2015)
12. H. Xiang, L. Fang, W. Fang, Y. Tang, C. Li, J. Eur. Ceram. Soc. **37**, 625 (2017)
13. C.L. Huang, J.Y. Chen, J. Am. Ceram. Soc. **92**, 379 (2009)
14. W.C. Tsai, Y.H. Liou, Y.C. Liou, Mater. Sci. Eng. B **177**, 1133 (2012)
15. D. Kajfez, A. Gundavajhala, Electron. Lett. **29**, 1936 (1993)
16. B.W. Hakki, P.D. Coleman, I.R.E. Trans, Microwave Theory Tech. **8**, 402 (1960)
17. J. Merikhi, H.O. Jungk, C. Feldmann, J. Mater. Chem. **10**, 1311 (2000)
18. M. Peymannia, A.S. Gorgani, M. Ghahari, F. Najafi, J. Eur. Ceram. Soc. **34**, 3119 (2014)
19. A. Nakatsuka, Y. Ikeda, Y. Yamasaki, N. Nakayama, T. Mizota, Solid State Commun. **128**, 85 (2003)
20. K.E. Sickafus, J.M. Wills, N.W. Grimes, J. Am. Ceram. Soc. **82**, 3279 (1999)
21. B. Liu, Y.H. Huang, K.X. Song, L. Li, X.M. Chen, J. Eur. Ceram. Soc. **38**, 3833 (2018)
22. B. Liu, L. Li, X.Q. Liu, X.M. Chen, J. Mater. Chem. C **4**, 4684 (2016)
23. Y. Zhai, Y. Tang, J. Li, L. Duan, C. Su, A. Cao, C. Jin, L. Fang, Ceram. Int. **46**, 28710 (2020)
24. W.B. White, B.A. DeAngelis, Acta A **23**, 985 (1967)
25. C.M. Álvarez-Docio, J.J. Reinosa, A.D. Campo, J.F. Fernández, J. Alloys Compd. **779**, 244 (2019)
26. O.N. Shebanova, P. Lazor, J. Solid State Chem. **174**, 424 (2003)
27. T. Yamanaka, M. Ishii, Phys. Chem. Miner. **13**, 156 (1986)
28. H. Cynn, S.K. Sharma, T.F. Cooney, M. Nicol, Phys. Rev. B **45**, 500 (1992)
29. M. Bouchard, A. Gambardella, J. Raman Spectrosc. **49**, 1477 (2010)
30. H. Shirai, Y. Morioka, I. Nakagawa, J. Phys. Soc. Jpn. **51**, 592 (1982)
31. S.J. Penn, N.M. Alford, A. Templeton, X.R. Wang, M.S. Xu, M. Reece, K. Schrapel, J. Am. Ceram. Soc. **80**, 1885 (1997)
32. W. Lei, W.Z. Lu, J.H. Zhu, X.H. Wang, Mater. Lett. **61**, 4066 (2007)
33. Y.H. Huang, B. Liu, K.X. Song, Ceram. Int. **44**, S125 (2018)
34. H.H. Guo, D. Zhou, C. Du, P.J. Wang, W.F. Liu, L.X. Pang, Q.P. Wang, J.Z. Su, C. Singh, S. Trukhanov, J. Mater. Chem. C **8**, 4690 (2020)
35. C. Du, H.H. Guo, D. Zhou, H.T. Chen, J. Zhang, W.F. Liu, J.Z. Su, H.W. Liu, J. Mater. Chem. C **8**, 14880 (2020)
36. J. Sun, K.M. Luk, I.E.E.E.T. Antenn, Propag. **65**, 4478 (2017)
37. A. Rajan, S.K. Solaman, S. Ganesanpotti, A.C.S. Appl, Electron. Mater. **3**, 2297 (2021)
38. H. Xiang, J. Kilpijärvi, S. Myllymäki, H. Yang, L. Fang, H. Jantunen, Appl. Mater. Today **21**, 100826 (2020)
39. D.H. Jin, B. Liu, K.X. Song, K.W. Xu, Y.H. Huang, C.C. Hu, Y.Y. Hu, J. Alloy Compd. **886**, 161141 (2021)